



# Pedigree Aerodynamic Shape Design of High-Speed Trains

P. Ji<sup>†</sup>, Z. L. Feng, and S. L. Liao

*School of Design, Hunan University, Changsha 410082, China*

<sup>†</sup>Corresponding Author Email: [jipengdesign@hnu.edu.cn](mailto:jipengdesign@hnu.edu.cn)

(Received May 26, 2022; accepted September 19, 2022)

## ABSTRACT

The aerodynamic performance of high-speed trains is closely related to their head shape. As each train set has its own modelling system, the aerodynamic shape design of head type of a high-speed train must follow a pedigree modelling approach. The train pedigree characteristics directly reflect its aerodynamic performance. The focus of this study is the extraction and application of the Shinkansen train pedigree features. First, large-scale differences in train head shapes are eliminated by dimensionless elimination. Second, the Shinkansen model pedigree features are extracted using similarity calculations. Finally, based on the constraint range of pedigree features on the new model shape, the concept head shape is designed with reference to the shape and surface parameters of high-speed trains, and its aerodynamic performance is verified. The results of the aerodynamic verification indicate that the concept design reduces the drag by more than 10% compared to the E2 Series base model. Additionally, the results demonstrate that the extraction and design application of train pedigree features can help a new train to develop its aerodynamic shape within its own pedigree modelling system, thus enabling the synergistic design of train shape and aerodynamic performance.

**Keywords:** Shinkansen; trains head-type design; Pedigree features; Aerodynamic shape; Shape synergy.

## NOMENCLATURE

$A$	windward surface area of the object	$V$	velocity of the gas relative to the body
$C$	force coefficient	$x$	coordinate in the x direction
$L_s$	length of streamlined train	$y$	coordinate in the y direction
$W_s$	width of train	$z$	coordinate in the z direction
$H_s$	height of train	$\hat{x}$	dimensionless coordinate in the x direction
$l_i$	shaped intersecting lines	$\hat{y}$	dimensionless coordinate in the y direction
$r$	correlation coefficient	$\hat{z}$	dimensionless coordinate in the z direction
<i>Greek letter</i>			
$\rho$	density of air		

## 1. INTRODUCTION

As the speed class of trains increases, the aerodynamic problems of train movement become increasingly significant (Zhang L. *et al.* 2016). The smoothness and comfort of high-speed trains are closely linked to their aerodynamic performance (Sun *et al.* 2021). The new model was designed by considering performance indicators such as aerodynamic loads in its shape (Song *et al.* 2015). The aerodynamic performance of a train is closely related to its head shape (Baker 2012; Tian 2009; Muñoz-Paniagua *et al.* 2014). Currently, the design process of China's high-speed train shape spectrum design is slow, thus posing higher requirements for research on spectrum design methods (Liu *et al.* 2019; Zhang *et al.* 2019). However, there are still

limitations in research that integrates aerodynamic performance and train shape, and there is a lack of research on design methods that combine the two factors after extracting the pedigree of the train shape characteristics (Yan *et al.* 2017).

Various studies have proposed a method for refining the shape of the train head from the point line using the characteristic line shape of the train as an entry point (Hou 2014). Other researchers have proposed the extraction of train profile genes based on profile gene signature lines (Huang and Dong 2021). A method for extracting shape parameters from train profiles and the maximum contour lines of longitudinal sections was proposed in previous studies (Zhang *et al.* 2013; Wu and Liu 2020). Additionally, a multi-objective cycle optimisation system for high-speed rolling stock can integrate the

existing design experience to generate multiple head options with excellent aerodynamic performance according to the design requirements for reference (Ding *et al.* 2021). Profile analysis involves comparing similarities between product shape features to determine the pedigree of features implicit in a product line (Person *et al.* 2008). Form design parameterisation provides ideas for the development of next-generation trains from the perspective of parameter-influenced design (Yao *et al.* 2021). The contouring parameters of the train shape gene can be used as a commonality of the train shape and they can provide a reference for the design of head shapes based on spectral characteristics.

In studies of product shape feature similarity extraction, the Pearson correlation coefficient calculation model was typically used to measure the degree of linear correlation between two feature nodes (Liu *et al.* 2013; Li *et al.* 2018b; Zhang *et al.* 2019; Zhang *et al.* 2016). As the model only reflects the degree of correlation between the two variables, handling the 3D coordinate parameters requires several calculations, which are slightly cumbersome and require optimisation of the model.

In contrast, in the iterative process of high-speed trains, the streamlined area varies significantly with the speed class, and the size of the parameters for different train head types cannot be compared directly. A spectral feature extraction method based on correlation calculations and dimensionless coordinates is proposed for the iterative process of high-speed trains, which is different from general products. First, to compare the section parameters of different size models uniformly, it is necessary to dimensionless the coordinates of the train surface points (Yue *et al.* 2020). Second, the surface feature points of the train were collected according to dimensionless coordinates, and the correlation coefficient of the dimensionless coordinate parameters was calculated for each group of feature points. Finally, according to the calculation results and the preset threshold, each group of feature points is divided into weights. The feature point weights reflect the similarity of the shape of its distribution area, and the high similarity area is extracted as the train shape spectrum feature.

The remainder of this paper is organised as follows. Section 2 presents the theoretical background, numerical and validation of the numerical simulation of air resistance; Section 3 presents the calculation of the train shape similarity; Section 4 presents the method of extracting train pedigree features based on dimensionless coordinates and correlation calculations; Section 5 presents the train shape design method and aerodynamic performance check calculations based on pedigree features; finally, the conclusions are presented in Section 6.

## 2. NUMERICAL SIMULATION AND MESH SETUP

The aerodynamic performance of high-speed trains is closely related to their shape. To investigate the

genetic characteristics of the aerodynamic shape of a train, it is necessary to start with the aerodynamic performance of the train; therefore, it is necessary to set up the computational domain and mesh in advance. The Japanese Shinkansen high-speed train is the most complex of all platforms in the world; therefore, the E2 series model was used for this study. The setup process is shown in Fig. 1.

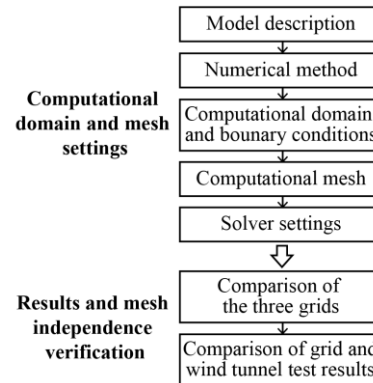


Fig. 1. Calculation flow chart.

### 2.1 Computational Domain and Mesh Settings

#### Model description

A three-car E2 series model with a scale of 1:1 was used for numerical simulations. The main geometric parameters of the model are a length,  $L$ , of 75.5 m, height,  $H$ , of 3.7 m, and width,  $W$ , of 3.38 m. In order to reduce the flow acceleration caused by the model's blocking effect on the computational domain, the ratio of blocking between the model and the computational domain was limited to less than 2% (Chen *et al.* 2017; EN 14067-4. 2009). The length of the calculation domain  $\pm Z$  direction is 50 m, and the geometric model is 0.2 m from the bottom of the calculation domain. The length of the calculation domain  $\pm Y$  direction is 100 m, with the model located in the middle. In the calculation domain  $\pm X$  direction, the geometric model is 100 m from the edge of the calculation domain in the  $X$  direction and 250 m from the edge of the  $+X$  direction to ensure that the flow field is fully formed in the calculation domain, as shown in Fig. 2 (Chen *et al.* 2017; Zhang *et al.* 2017).

#### Numerical method

Large Eddy Simulation (LES) is an effective way to simulate the flow field around trains; however, it is computationally expensive (Hemida and Krajnovic 2009; Hemida *et al.* 2012; Krajnovic *et al.* 2012). The Reynolds-averaged Navier–Stokes (RANS) model requires fewer computational resources for its calculations, but it is unable to simulate the large-scale separated flow field around the train accurately. Owing to the extremely large scale and complex shape of high-speed trains, the application of LES in fields with high Reynolds numbers is limited by the computational resources required. The hybrid the improved delayed detached-eddy simulation (IDDES) method of RANS and LES achieves a good balance between numerical accuracy and computational cost, and this method

has been widely used in the study of train aerodynamics (Wang *et al.* 2017; Guo *et al.* 2018; Guo *et al.* 2019; Zhang J. *et al.* 2016). Solver using the SST k- $\omega$  based solver IDDES formulation with a combination of delayed detached-eddy simulation (DDES) and wall-modeled LES (WMLES) to overcome the limitations of modelled stress depletion (MSD) and grid-induced separation (GIS) and reduce the near-wall flow Reynolds number. The IDDES method was selected for the numerical simulation of the aerodynamic drag of a three-car train in an open-line operation.

*Computational domain and boundary conditions*

The calculation area is shown in Fig. 2, and the train is defined to be running along the -X direction. To simulate the operation of a train, it is assumed that the train is stationary and air is blown into the calculation domain from opposite directions at the same speed (Tian 2007; Tan *et al.* 2018). The speed entrance boundary (surface BADC) was set at 97.22 m/s (350 km/h). The static pressure at the pressure outlet (surface EFGH) was equal to the ambient pressure, which is 0 Pa in the simulation. The ABFE surface at the bottom of the calculation domain was set up as a sliding wall surface, moving at the same speed as the air velocity at the velocity inlet to achieve relative motion between the ground and the train (Tan *et al.* 2018). The calculation domain width direction faces and top faces BCGF, AEHD, and CDHG were set to the Wall, as shown in Fig. 2.

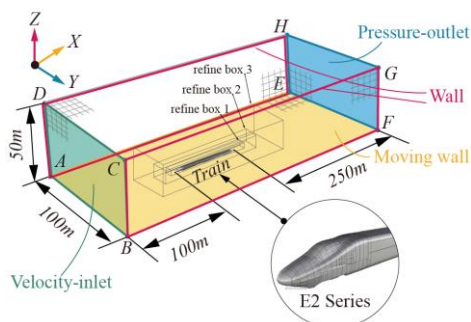


**Fig. 2. Calculation area in the open lines.**

*Computational mesh*

Mesh generation was conducted in the commercial software STAR-CCM+ developed by Siemens using the Trimmer and Prism Layer Mesher for mesh discretisation of the calculation area (Liang *et al.* 2020). In the settings, the percentage of base of the maximum cell size in space is 200, and the number of prism layers is 5. The value in the base size of the object surface grid is 1 m and the relative minimum size has the property percentage of base 2, which controls the minimum grid to 0.05 m. The spatial grid is locally refined to improve the grid resolution; in particular, to enable the IDDES solver to capture the details of the turbulent structure in the train wake area at 10, 15, and 20 m from the train in the -X direction; 10, 20, and 40 m from the train in the +X direction; 0.5, 5, and 15 m from the train in the  $\pm Y$  direction; 1, 10, and 20 m from the train in the +Z direction; 0.2 m from the train in the -Z

direction, generating three sets of grid encryption zones parallel to the calculation domain. The first layer of mesh on the surface is 1 mm thick and it has a growth rate of 1.15, and it is called the medium mesh. In the mesh independence test, coarse mesh and fine mesh were built with reference to the medium mesh, with growth rates of 1.05 and 1.2 for coarse mesh and fine mesh, respectively. As the overlapping mesh does not require any modification after the initial mesh is generated, motion modelling uses an overlapping mesh. The numbers of coarse, medium, and fine mesh meshes are  $7.3 \times 10^6$ ,  $12.4 \times 10^6$ , and  $16.5 \times 10^6$ , respectively, for the open line operating conditions of the train, as shown in Fig. 3.

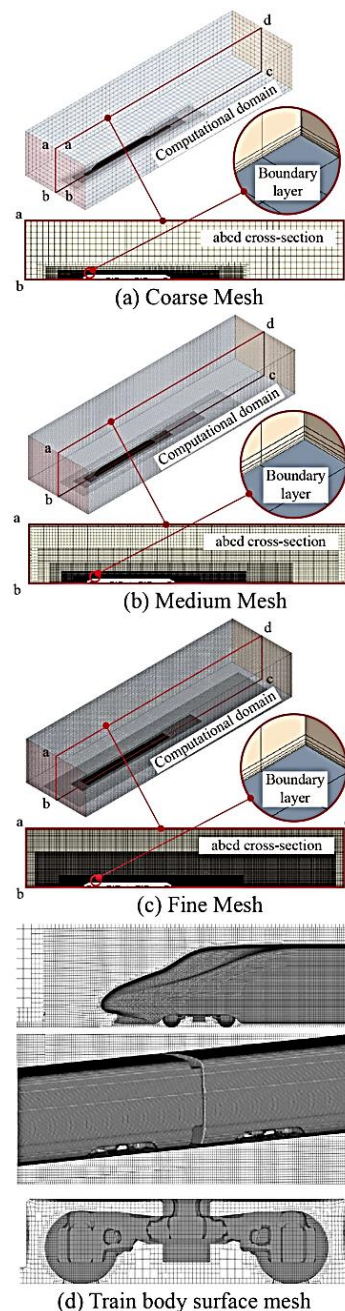


**Fig. 3. Computational (a) coarse, (b) medium, (c) fine meshes in the open lines and (d) body, (e) Bogie surface grid.**

*Solver settings*

The solution was obtained using the IDDES solver, separating the pressure-velocity coupling method in the flow solver. The discretisation of the convective term is based on a hybrid format switching between the bounded central difference scheme (BCDS) and the second-order windward scheme, using BCDS for 15% of the entire domain. A second-order windward scheme is used (Ashton 2017; Xia *et al.* 2017). In the transition simulation, the time term was a second-order implicit scheme. Some studies have demonstrated that minor violations of the Courant number requirement are unlikely to have a significant effect on the flow field (Flynn *et al.* 2014; Flynn *et al.* 2016). For coarse, medium, and fine meshes, the discrete time steps are  $0.025t^*$ ,  $0.02t^*$ , and  $0.015t^*$ , respectively, where  $t^*$  is the dimensionless time equal to  $v \cdot \Delta t / H$ . The time step was chosen such that the local Courant number was less than 1, and the Courant number exceeded 1 only in a very small part of the grid. The above time steps are sufficient to resolve the nonconstant turbulent flow around the train, and the IDDES method can be used to present the flow structure around the train at higher Reynolds numbers (Ashton 2017).

**2.2 Aerodynamic Calculation Results and Mesh Independence Verification**

As the flow field around the train takes time to reach a fully turbulent state during the simulation, a reasonable reference must be proposed to assess whether the flow field has reached an acceptable state. The resistance factor,  $C$ , is given in Ep. (1).

$$C = \frac{F}{(0.5\rho V^2 A)} \tag{1}$$

Table 1 was obtained by calculating the drag coefficients for the three meshes, where  $C$  is the total drag coefficient for the three-car formation of the mesh:  $C = 0.388, 0.388, \text{ and } 0.405$  for the coarse, medium, and fine meshes, respectively. Using the medium mesh as a reference, the relative error of the drag coefficient for the three vehicles is 0 for the coarse mesh total drag and 4.3% for the fine mesh. By comparing the resistances, the medium mesh setting is reasonable, and the calculation results are similar to those of the other settings.

To validate the numerical model, CFD was

compared with the results of wind tunnel tests. The wind tunnel test site was the FL-13 wind tunnel of the China Aerodynamic Research and Development Centre, and the test object was Chinese CRH2A (Zhang *et al.* 2018; Zhang *et al.* 2016a; Li *et al.* 2018a). Currently, the FL-13 wind tunnel is the largest low-speed wind tunnel in Asia, with a wind speed range of 20–100 m/s. The wind tunnel test setup is illustrated in Fig. 4 (Li *et al.* 2018a). Because the CRH2A model was introduced to the Shinkansen E2 Series in Japan, the geometry was the same as that of the E2 Series (Li and An 2007). The test air velocity were 97.22 m/s. The boundary conditions in the numerical calculation are the same as those in the wind tunnel test, using the medium mesh as a reference. The comparison between the calculation results and the wind tunnel test results is summarized in Table 3 (Zhang *et al.* 2018; Zhang *et al.* 2016). Consequently, the computational accuracy of the medium mesh is sufficient for engineering research.



**Fig. 4. Experimental train model setup.**

**3. TRAIN SHAPE SIMILARITY CALCULATION**

**3.1 Correlation Calculations and Dimensionless Processing**

The current Pearson correlation coefficient calculation model can only be used to measure the degree of linear correlation between two feature nodes (Zhang *et al.* 2016; Zhang *et al.* 2019).

**Table 1 Drag coefficient for open made operation of trains**

Mesh density	Total number, $10^6$	First train $C$	Middle train $C$	Last train $C$	All $C$	Result error
Coarse mesh	7.3	0.145	0.083	0.160	0.388	0%
Medium mesh	12.4	0.145	0.083	0.160	0.388	0%
Fine mesh	16.5	0.146	0.084	0.176	0.405	4.3%

**Table 2 Drag coefficient from the numerical calculations and wind tunnel tests.**

	First train $C$	Middle train $C$	Last train $C$	All $C$
Wind tunnel	0.143	0.08	0.162	0.385
Medium mesh	0.145	0.083	0.160	0.388
Differences	-1.4%	-3.6%	+1.2%	-0.8%

$$r = \frac{\sum_{i=1}^n (x_i - \bar{x}) \sum_{i=1}^n (y_i - \bar{y})}{\sqrt{\sum_{i=1}^n (x_i - \bar{x})^2} \sqrt{\sum_{i=1}^n (y_i - \bar{y})^2}} \quad (2)$$

where  $r$  is the correlation coefficient between the variables  $x$  and  $y$ . A threshold  $[r]$  is set for this, and when the value of  $r$   $[-1,1]$  exceeds the threshold, the two variables are considered linearly correlated; the larger the absolute value of  $r$ , the stronger the correlation.

During the iterations of the head shape of the high-speed trains, the streamlined length increases significantly as the speed class increases. Different sizes of models have different locations for the same feature area; therefore, a uniform standard needs to be established for the comparison of different size train models. The original calculation model can only reflect the degree of correlation between the two variables, and the 3D coordinate parameters for the feature points must be calculated in each of the three plane views so that the final calculated values are small in absolute value and low in precision owing to the three multiplication relationships. Therefore, the existing computational model needs to be improved, and a method for extracting pedigree features from the aerodynamic shapes of high-speed trains needs to be developed.

### 3.2 Dimensionless to Eliminate Large-Scale Differences in Trains

Owing to the large variation in the size of the deformation area during the high-speed train iterations, head-type parameters of different magnitudes cannot be directly compared. Therefore, a dimensionless quantisation method based on the point weights of the train contour elements was proposed to reflect the similarity of each region of the train contour.

First, the full range of the Shinkansen models was modelled using the Rhino software, and the spatial coordinate system of the train models was unified. The direction of the train streamline length is set as the X-axis, the position of the end of the streamline is located at coordinate  $x = 0$ , the tip of the nose is located in the X-positive direction, the centre line of the train symmetry surface is located at coordinate  $y = 0$ , and the train track surface is located at coordinate  $z = 0$ , as shown in Fig. 5.

The surface point coordinates of the train model after unification of the coordinate system are dimensionless to obtain the following relationship:

$$\begin{aligned} \hat{x} &= \frac{x}{L_s}, \\ \hat{y} &= \frac{y}{\frac{1}{2}W_s}, \\ \hat{z} &= \frac{z}{H_s}, \end{aligned} \quad (3)$$

where  $\hat{x}$ ,  $\hat{y}$ , and  $\hat{z}$  are the dimensionless coordinate values;  $x$ ,  $y$ , and  $z$  are the original coordinate parameters of the train surface points;  $L_s$  is the

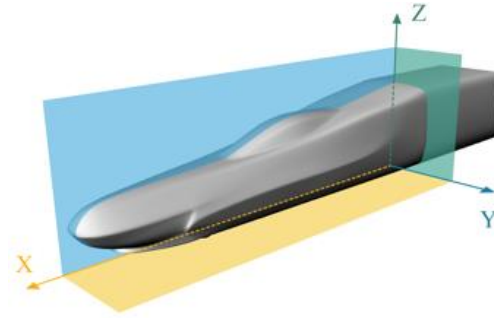


Fig. 5. Spatial coordinate system for train models.

length of the train streamline;  $W_s$  is the width of the entire train;  $H_s$  is the height of the entire train.

After dimensionless processing, the coordinate parameters of all surface points of the train are changed from absolute to relative values, and different size models can be compared for similarity of shape, regardless of the size difference.

For the entire Shinkansen train, the shape surface feature points of the train were collected based on the coordinates after the train became dimensionless. Because the trains were symmetrical in shape from left to right, with the head and tail cars having the same geometric shape, only the left-hand streamlined area shape of the head car was sampled. The Shinkansen E5 series model is shown as an example to present the collection method and results visually.

First, the train streamline area length  $L_s$  was divided into 11 equal parts to obtain 11 shape intersecting lines  $l(i = a, b, \dots, k)$ , as shown in Fig. 6(a).

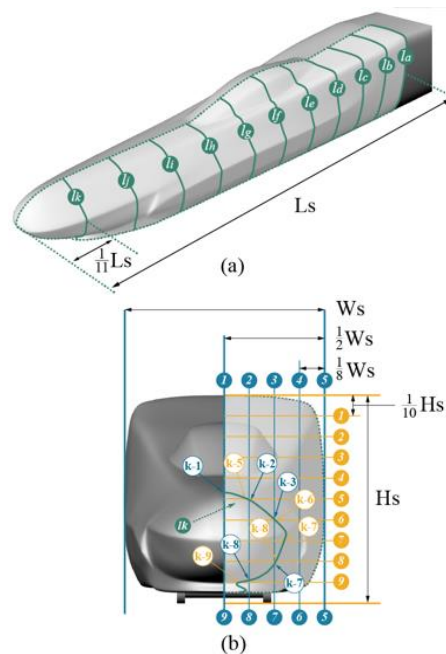
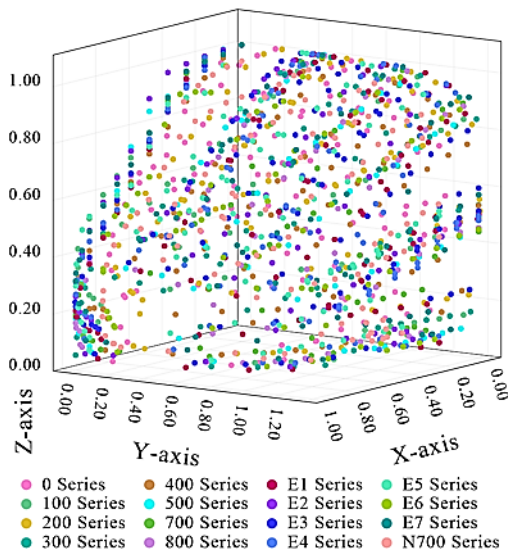


Fig. 6. Train surface characteristics point layout (a) profile intersecting lines (b) the specific marking method.

Second, in the front view of the train, five vertical lines were made from the centre line of the train to the outermost side of the train equally divided by  $\frac{1}{2}W_s$  on the right side, with the upper side of the vertical lines from left to right marked in blue 1 to 5, and the lower side marked in blue 9 to 5. Horizontal lines were made from the rail surface to divide  $H_s$  into 10 equal parts, from top to bottom. The horizontal lines were orange 1 to 9, in order. The specific marking method is shown in Fig. 6(b). The final grid in the front view of the train is a grid of lines of equal length and width.

Finally, by marking the intersection of the isometric shape intersecting lines,  $l_i$ , and the front-view aspect contour grid, the train surface feature points were collected, and the dimensionless coordinate values of each set of feature points were consistent in the X direction and varied only in the Y and Z directions. The specific marking method used the green line  $l_k$  as an example, which intersected the orange horizontal lines 6, 7, 8, and 9 to obtain nodes orange k-6, k-7, k-8, and k-9, respectively.  $l_k$  intersected the centre line only once, marking the node with the upper side marker, blue k-1; second line twice, with blue k-2 on the upper side and blue k-8 on the lower side; third line twice, with blue k-3 on the upper side and blue k-7 on the lower side. The ten nodes formed by  $l_k$  intersecting with this grid were the feature points on the  $l_k$  curve, as shown in Fig. 6(b).

The intersection of each coherent line with the grid of the length and width contours in the front view was marked in 3D coordinates on the surface of the train to form a map of the distribution of feature points on the entire train surface, as shown in Fig. 7.



**Fig. 7. Distribution of characteristic points of the Shinkansen in the dimensionless coordinate system.**

Because the number of intersections between the shape intersecting lines and the grid of different models might be different, to ensure the feasibility

of the calculation, only common feature points to the entire Shinkansen model were retained to obtain a map of those in the dimensionless coordinate system. Figure 7 shows that the feature points of the 16 Shinkansen models have a tendency to cluster in the same coordinate system. To clarify the similar feature points and their locations, the correlation between the parameters of each group of feature points was calculated.

### 3.3 Train Profile Similarity Calculation

To calculate the degree of correlation of the coordinate parameters of the surface feature points, the modified model based on the Pearson correlation coefficient calculation model is expressed as follows:

$$r = \frac{\sum_{i=1}^n x_i^* \cdot \sum_{i=1}^n y_i^* \cdot \sum_{i=1}^n z_i^*}{\sqrt{\sum (x_i^*)^2} \sqrt{\sum (y_i^*)^2} \sqrt{\sum (z_i^*)^2}} \quad (4)$$

$$x^* = \begin{cases} \hat{x} - \bar{x}, & \hat{x} - \bar{x} \neq 0 \\ 1, & \hat{x} - \bar{x} = 0 \end{cases}$$

$$y^* = \begin{cases} \hat{y} - \bar{y}, & \hat{y} - \bar{y} \neq 0 \\ 1, & \hat{y} - \bar{y} = 0 \end{cases} \quad (5)$$

$$z^* = \begin{cases} \hat{z} - \bar{z}, & \hat{z} - \bar{z} \neq 0 \\ 1, & \hat{z} - \bar{z} = 0 \end{cases}$$

In Eq. (4),  $r$  is the absolute value of the product of the overall correlation coefficients of coordinate node  $i$  in the X, Y, and Z coordinate directions, taking values in the range  $[0,1]$ ;  $\hat{x}$ ,  $\hat{y}$ , and  $\hat{z}$  are the dimensionless coordinate parameters of each feature point.  $x^*$ ,  $y^*$ , and  $z^*$  are the values obtained by the feature points in the X, Y, and Z coordinate directions, respectively. This model for calculating the correlation coefficient excludes the case in which the monomial is set to zero during the calculation and the  $r$  value is subsequently set to zero.

By substituting the dimensionless coordinates of each group of feature points into the calculation, the corresponding result of  $r$  value is the correlation coefficient of the coordinate parameters of the group of feature points, and the calculation results can be weighted according to different thresholds as follows:  $0.8 \leq r < 1$  is highly correlated;  $0.6 \leq r < 0.8$  is moderately high correlation;  $0.4 \leq r < 0.6$  is moderately correlated;  $0.2 \leq r < 0.4$  represents moderate and low degree correlation. When  $0 \leq r < 0.2$ , the group of feature points is not considered to be correlated when quantifying the train profile similarity owing to the low correlation.

### 3.4 Algorithm Validation

The correlation coefficients for the dimensionless coordinate parameters of the train surface features were calculated separately using a modified before-and-after calculation method, and the results were compared for verification.

In Fig. 8(a), the green and blue attributes of the feature points are marked as 1 and 2, respectively. For instance, feature point green a-1 was relabelled as a1-1, and feature point blue a-1 was relabelled as a2-1. The feature points are arranged in ascending

order according to letters and numbers in the horizontal coordinates, and the calculation results of the modified and pre-modified methods are marked in the vertical coordinates to form red and green point clouds, respectively. To compare the consistency of the two methods, the cube roots of the values calculated by the pre-modified method were taken and marked on the graph to obtain blue point clouds.

Comparing the red and blue point clouds in Fig. 8(a), we can observe that the final calculation results of the two methods are the same, which verifies the feasibility of the improved calculation method. Combined with the red and green point clouds in Fig. 8(b) the division of feature point weights, it can be observed that the improved method (red points clouds) calculates a wider range of numerical fluctuations, which facilitates the separation of different weighted feature points and the extraction of train pedigree features.

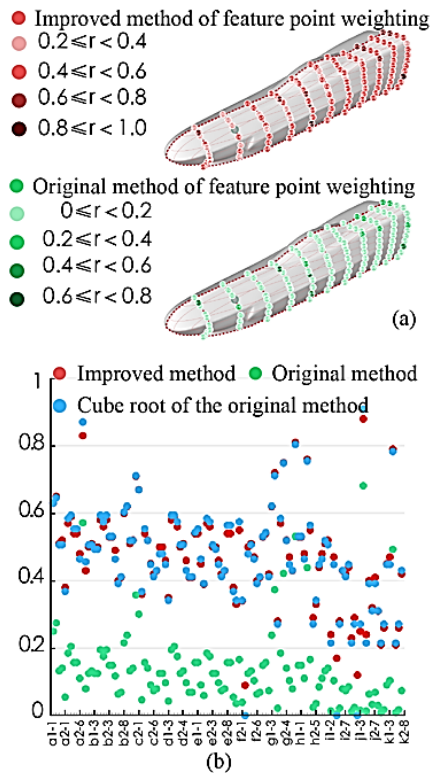


Fig. 8. Comparison of results before and after improving the method.

#### 4. EXTRACTION OF THE SHINKANSEN PEDIGREE FEATURE

##### 4.1 Train Shape Area Division

The train shape area is divided according to the train shape layout, where  $L_s$  is the length of the train streamline. The nose tip point to one-third of  $L_s$ , containing the part of the head shape owing to the hook and buffer structure triggered by the shape change, was defined as the nose area, as shown in Fig. 9.

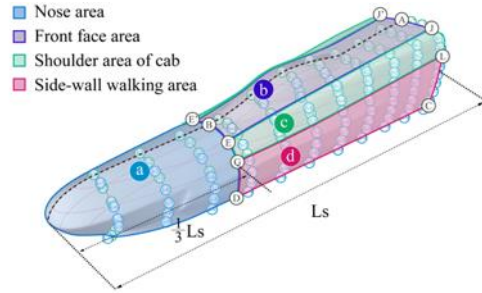


Fig. 9. Quantification and division of the Shinkansen shape similarity.

Point L was the position of the midpoint of the turn of the roof and sidewalls, and GL was the extension of the junction line between the roof and sidewalls of the train carriage on the streamlined. Points J, I, and E were trisecting curves GG', NN', and LL', respectively, with points J and E being 2/5 of the way up curves LA and GB, respectively, near the side walls. Based on the above division, area b is defined as the front face area, area c is the shoulder area of the cab, and area d is the sidewall walking area. Each region can be divided into anterior, middle, and posterior segments, except for the nasal area.

##### 4.2 Pedigree Feature Area Extraction and Modelling Analysis

The division of feature point weight and shape similarity quantification for Shinkansen models is based on predefined thresholds, as shown in Fig. 10. When  $0.8 \leq r < 1$ , only three groups of feature points appear on the front face area, on the lower and middle parts of the side-wall walking area, and at the rear area of the side-wall walking area, with no significant areas of feature point clustering. When  $0.6 \leq r < 0.8$ , scattered areas of agglomeration at the rear area of the front face area, front section of the nose area, and side-wall turning area are highly similar. When  $0.4 \leq r < 0.6$ , large areas of agglomeration at the cab section of the front face area, rear area of the side-wall turning area and side-wall walking area are moderately similar. When  $0.2 \leq r < 0.4$ , a few areas of clustered feature points appear in the nose area, front face area, cab section of the front face area, and shoulder area of the cab, which are low in similarity.

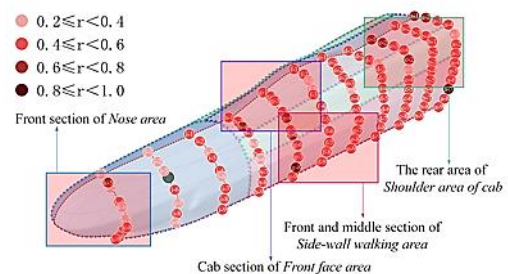
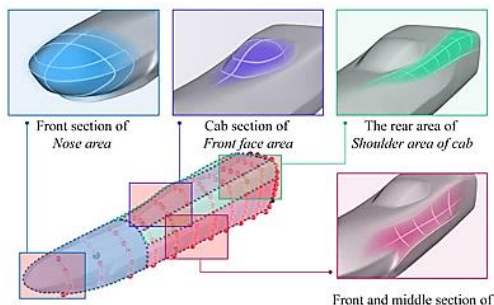


Fig. 10. Regional distribution of high similarity of the Shinkansen shape.

Based on the results of the similarity analysis, the Shinkansen pedigree feature areas can be

pinpointed to the front section of the nose, cab section of the front face, front and middle sections of the side-wall walking and rear areas of the shoulder area of the cab. As the iterative process of the entire Shinkansen model had gone through four speed classes, the E5 Series, a high-speed class model, was selected for the reduction of pedigree features in each area to ensure that the extracted features can provide a reference for the aerodynamic shape design of the new train. The front section of the nose area was flattened in the form of a duckbill. The cab section of the front face area has a teardrop canopy with an overall protrusion from the curved surface of the front face area. The shoulder area of the cab was clearly turned, and the turning vanishing point was articulated at the point where the front face met the nose area. The side-wall walking area has a distinctive concave and turning line, and when combined with the shoulder area of the cab, they present a winged aerodynamic layout.



**Fig. 11. Summary of the Shinkansen pedigree features.**

### 4.3 Comparison of Pedigree Feature Weights

The weight of each profile region was evaluated according to the proportion of feature points under different thresholds in each region and finally integrated to obtain the weight coefficients of each region, which can be referred to in the design of new models to retain their features in proportion. The weighting coefficients for different thresholds in each area are listed in Table 3.

## 5. VERIFICATION OF SHAPE DESIGN AND AERODYNAMIC PERFORMANCE CALCULATIONS BASED ON PEDIGREE FEATURES

### 5.1 Conceptual Design of High-Speed Train's Head Shape

Based on the results of the Shinkansen pedigree feature extraction, the new train needs to retain the

Shinkansen shape in the front section of the nose area, cab section of the front face area, rear area of the shoulder area of the cab, as well as front and middle sections of the side-wall walking area so that its shape does not depart from its own styling system. To test the feasibility of optimising the aerodynamic shape of the train under this styling system, a conceptual solution head design was developed based on the E2 series control parameters for the low-speed class train, using the above-mentioned regional features of the high-speed class train as a reference. The parameters of the E2 system are as follows: the length of the head train is 27.5 m and the streamlined length is 9.1 m.

First, referring to the E5 series shape element point layout in the dimensionless coordinate system, the coordinate migration for the E2 series shape element points of the front section of the nose area, cab section of the front face area, turning of the shoulder area of the cab, as well as front and middle sections of the sidewall walking area were performed, as shown on the left in Fig. 12. Second, the relocated shape element points were restored to the original dimensional coordinate system of the E2 series and the above area surfaces were modulated to enhance the expression of its pedigree features. Finally, the overall parameters were adjusted according to the consistency of the surfaces around the bogie and the coordination of streamlined surfaces of the head train to obtain a conceptual shape design.

### 5.2 Analysis of Conceptual Shape Design of Aerodynamics Performance

To evaluate the aerodynamic performance of the concept model in actual open lines, the concept model was subjected to numerical calculations for the open lines using the same calculation setup. Fig. 13 shows a pressure cloud of the train body. As shown in the diagram, the hysteresis zone appears in the nose section of the head train (red section) and is smaller in the concept solution compared to the E2 and E5 Series. The positive pressure zone at the lower edge of the cab front window in the concept design has a smaller range of pressure variation and is more evenly spaced. The positive pressure zone at the upper edge of the cab front window is not significantly different from the negative pressure zone at the top of the cab in the front face area. Of the three trains, the concept design appears to have a smoother and less extensive positive pressure zone in the rear part of the car. On balance, the concept's shape is superior in terms of aerodynamic performance.

Figure 14 shows a cloud of the velocity distribution of the flow field for the concept design, E2 Series, and E5 Series in open lines, with the body showing

**Table 3 Statistical table of the weighting of each shape area**

	0.2–0.4	0.4–0.6	0.6–0.8	0.8–1.0
Nose area	50.00%	38.89%	5.56%	0%
Front face area	11.11%	75.00%	13.89%	0%
Shoulder area of cab	19.23%	69.23%	11.54%	0%
Side-wall walking area	4.88%	90.24%	0%	4.88%

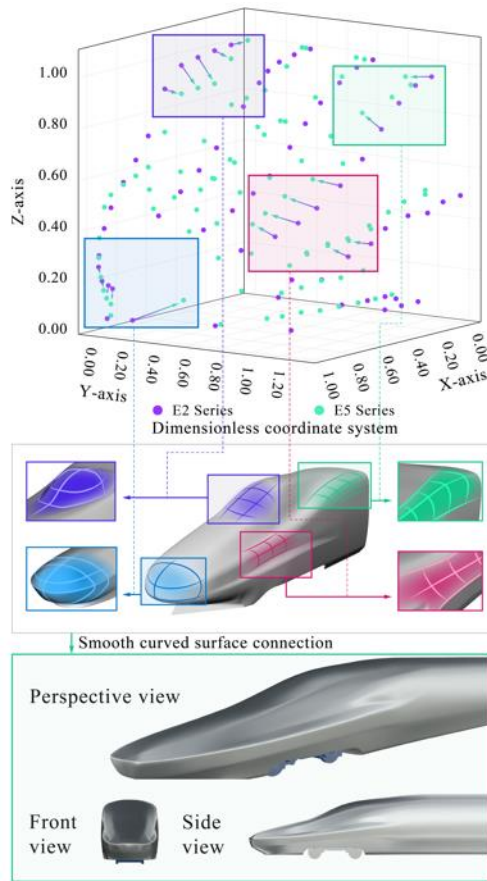


**Fig. 12.** Method of train's head shape design.

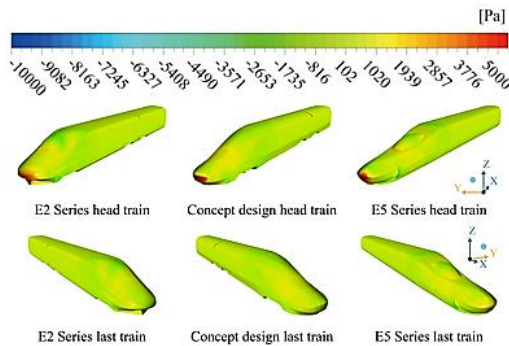


**Fig. 13.** Concept design body pressure cloud map in open lines.

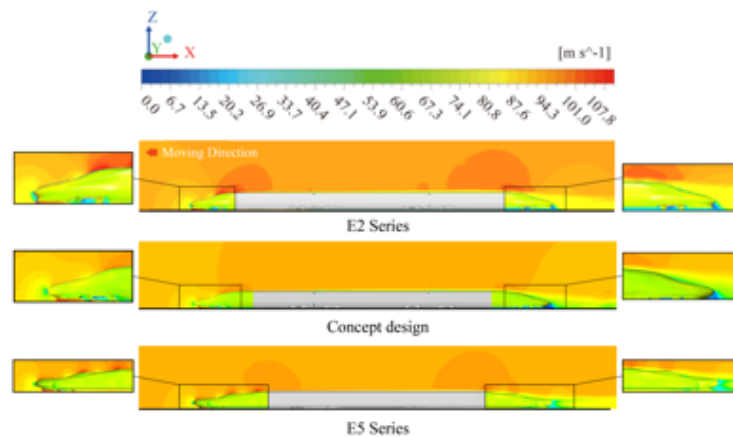


**Fig. 14.** Concept design Flow velocity cloud map in open lines.

the pressure distribution. The stagnation zone formed by the airflow reaching the nose-point is significantly smaller compared to that of the E2 Series (cyan in the E2 Series, green in the concept design). Smaller and more homogeneous air flow variation occurs at the lower edge of the cab's front window compared to those of the E2 and E5 Series. The acceleration zone at the upper edge of the cab is smaller and the transition in gas flow velocity is smoother. The concept design has a greater range of negative pressure zones in the vortex region of the tail car, which is better than that of the E2 Series and close to the level of the E5 Series. Overall, the aerodynamic performance of the concept is better than that of the E2 Series, and in some areas of the shape, it is better than that of the E5 Series. In comparison with the E5 Series, the concept has a smaller area of low-speed vortex generation at the rear of the last train, and the speed variation is clearly reduced.

After calculating the concept design and E2 Series in the open lines, the results for the three-train aerodynamic drag for both models were obtained and are listed in Table 4. The concept design has an aerodynamic resistance factor of  $C = 0.355$ , which represents a drag reduction of more than 10% in relation to the E2 Series.

The analysis of the aerodynamic performance in the open lines shows that the concept is operationally feasible and offers significant improvements in aerodynamic performance over the E2 Series.

**Table 4** Aerodynamic calculations results of the concept design in the open lines

	E2	Concept	E5
$C_x$	0.382	0.355	0.330
Percentage variance	0.0%	-7.1%	-13.6%

## 6. CONCLUSION

In this study, the large-scale difference in the comparison process of the train head shape was eliminated using a dimensionless method to explore the commonness of the train's aerodynamic shape.

Extracting the Shinkansen shape pedigree features and referring to existing high-speed class trains to design a concept shape under the Shinkansen pedigree styling system. The specific conclusions are as follows:

(1) Based on the dimensionless train coordinate system, large-scale differences in the trains can be eliminated. It is more conducive to explore the commonalities in the aerodynamic shapes of trains between large-scale ranges of trains.

(2) Based on the similarity calculation, it can be established that the Shinkansen pedigree features are concentrated in the front of the nose area, cab section of the front face area, turning of the shoulder area of the cab, and front-middle section of the side-wall walking area. The thresholds for feature parameters in different areas can guide the codesign of the aerodynamic performance and train shape.

(3) The following adjustments to the areas mentioned above can lead to better aerodynamic performance of the train shape: larger and wider nose shape in the nose area; the cab section of the front face area is located further back; lower position of the turning of the shoulder area of the cab; larger curve turning in the side-wall walking area.

This study contributes to the design and optimisation of high-speed train shapes while retaining the characteristics of the train pedigree model, enabling further optimisation of aerodynamic performance with low-performance indicator trains. For existing low-speed models, optimisation ideas are provided to enhance the family style of Chinese high-speed trains while improving aerodynamic performance. The final result is a synergistic design that considers both the pedigree shape and aerodynamic performance of the train.

The shortcoming of the method proposed in this study is that it focuses more on the optimisation of existing low performance trains. The relationship between tail lift and shape design is also an important factor in evaluating the merits of aerodynamic shapes and will need to be taken into account more in future research.

#### ACKNOWLEDGEMENTS

The authors would like to acknowledge the financial support from the Natural Science Foundation of Hunan Province (Grant number 2022JJ40064).

#### REFERENCES

Ashton, N. (2017). Recalibrating Detached-Eddy Simulation to eliminate modelled- stress depletion. *Recalibrating Detached-Eddy Simulation to eliminate modelled- stress depletion*, 27-35.

Baker, C. (2012). The flow around high speed

trains. *Journal of Wind Engineering & Industrial Aerodynamics* 98, 277-298.

Chen, Z. W., T. H. Liu, Z. H. Jiang, Z. J. Guo and J. Zhang (2017). Comparative analysis of the effect of different nose lengths on train aerodynamic performance under crosswind. *Journal of Fluids And Structures* 78, 69–85.

Ding, S. S., D. W. Chen and J. L. Liu (2021). Development and prospects of high-speed trains in China. *Acta Mechanica Sinica* 53, 35-50.

EN 14067-4. (2009). *Railway Applications - Aerodynamics - Part 4: Requirements and Test Procedures for Aerodynamics on Open Track*. European Committee for Standardization. Brussels Belgium.

Flynn, D., H. Hemida and C. Baker (2016). On the effect of crosswinds on the slipstream of a freight train and associated effects. *Journal of Wind Engineering and Industrial Aerodynamics* n 156, 14-28.

Flynn, D., H. Hemida, D. Soper and C. Baker (2014). Detached-eddy simulation of the slipstream of an operational freight train. *Journal of Wind Engineering and Industrial Aerodynamics* n 132, 1-12.

Guo, Z. J., T. H. Liu and Z. W. Chen (2019). Numerical study for the aerodynamic performance of double unit train under crosswind. *Journal of Wind Engineering and Industrial Aerodynamics* 191, 203-214.

Guo, Z. J., T. H. Liu, Z. W. Chen and T. Z. Xie (2018). Comparative numerical analysis of the slipstream caused by single and double unit trains. *Journal of Wind Engineering and Industrial Aerodynamics* 172, 395-408.

Hemida, H. and S. Krajnovic (2009). Development and prospects of high-speed trains in China. *In book: Computational Fluid Dynamics*, 451-456.

Hemida, H., C. Baker and G. J. Gao (2012). Development and prospects of high-speed trains in China. *Proceedings of the Institution of Mechanical Engineers Part F Journal of Rail and Rapid Transit* 228, 25-36.

Hou, G. H. (2014). Establishment and Application of Product Modelling Gene Intention Model. *Journal of Machine Design* 31, 105-108.

Huang, Z. J. and S. Y. Dong (2021). Application and Extraction of Exterior Appearance Gene of CRH High-speed Train Based on DFA. *Packaging Engineering* 42, 249-255.

Krajnovic, S., P. Ringqvist, K. Nakade and B. Basara (2012). Large eddy simulation of the flow around a simplified train moving through a crosswind flow. *Journal of Wind Engineering and Industrial Aerodynamics* 110, 86-99.

- Li, F. and Q. An (2007). The development of high-speed trainsets at home and abroad. *Electric Locomotives & Mass Transit Vehicles* 05, 1–5.
- Li, X. F., D. Zhou, L. R. Jia and M. Z. Yang (2018a). Effects of yaw angle on the unsteady aerodynamic performance of the pantograph of a high-speed train under crosswind. *Journal of Wind Engineering and Industrial Aerodynamics* 182, 49–60.
- Li, Y., C. F. Lu, X. J. Liu, Z. Sheng and G. Z. Chai (2018b). Gene network model of automobile shape design. *Computer Integrated Manufacturing System* 24, 1249-1260.
- Liang, X. F., X. B. Li, C. Guang, B. Sun, Z. Wang, X. H. Xiong, J. Yin, M. Z. Tang, X. L. Li and S. Krajnović (2020). On the aerodynamic loads when a high speed train passes under an overhead bridge. *Journal of Wind Engineering and Industrial Aerodynamics* 202, 104208.
- Liu, X. J., Y. Sun, J. F. Wu and S. W. Cheng (2013). Product gene regulatory network model and its assistance to the design process. *Computer Integrated Manufacturing System* 19, 1463-1471.
- Liu, Y., J. R. Wu and X. Liu (2019). Research on the Application of Design Geometry in High-speed Train Appearance Design. *Art & Design* 11, 126-127.
- Muñoz-Paniagua, J., J. García and A. Crespo (2014). Genetically aerodynamic optimization of the nose shape of a high-speed train entering a tunnel. *Journal of Wind Engineering & Industrial Aerodynamics* 130, 48-61.
- Person, O., J. Schoormans and D. Snelders and T. M. Karjalainen (2008). Should New Products Look Similar or Different? The Influence of the Market Environment on Strategic Product Styling. *Design Studies* 29, 30-48.
- Song, Y., P. B. Wu and L. Jia (2015). Strength Analysis on Head-car Body of Electrical Multiple Units. *China Mechanical Engineering* 26, 553-559.
- Sun, Z. X., Y. F. Yao, D. L. Guo, G. W. Yang, S. B. Yao, Y. Zhang, D. W. Chen, G. B. Li, K. M. Shang and L. Jia (2021). Research progress in aerodynamic optimization of high-speed trains. *Chinese Journal of Theoretical and Applied Mechanics* 53, 51-74.
- Tan, X. M., Z. G. Yang, X. L. Wu and J. Zhang (2018). Vortex structures and aeroacoustic performance of the flow field of the pantograph. *Journal of Sound and Vibration* 432, 17-32.
- Tian, H. Q. (2007). *Train aerodynamics*. Beijing: China Railway Publishing House.
- Tian, H. Q. (2009). Formation mechanism of aerodynamic drag of high-speed train and some reduction measures. *Journal of Central South University of Technology* 1, 166-171.
- Wang, S. B., J. R. Bell, D. Burton, A. H. Herbst, M. C. Thompson and J. Sheridan (2017). The performance of different turbulence models (URANS, SAS AND DES) for predicting high-speed train slipstream. *Journal of Wind Engineering and Industrial Aerodynamics* 165, 46–57.
- Wu, Y. F. and X. J. Liu (2020). Aided rapid design of the maximum contour line of the longitudinal section of the high-speed train head. *Packaging Engineering* 41, 197-201.
- Xia, C., H. F. Wang, X. Z. Shan, Z. G. Yang and Q. L. Li (2017). Effects of ground configurations on the slipstream and near wake of a high-speed train. *Journal of Wind Engineering and Industrial Aerodynamics* 168, 177-189.
- Yan, Y. C., Z. Tang, N. Gao and C. Wang (2017). Development of research on aerodynamics of high-speed rails in China. *Engineering Sciences* 34, 105-112.
- Yao, S. B., D. J. Chen, S. S. Ding and S. J. Pang (2021). Multi-Objective Aerodynamic Optimization Design of High-Speed Maglev Train Nose. *China Railway Science* 42, 98-106.
- Yue, L. Z., X. Xing and G. L. Shi (2020). The nature analysis and method selection of non-dimensional indicators. *Statistics and Information Forum* 35, 3-9.
- Zhang, J., J. J. Li and H. Q. Tian, G. J. Gao and S. John (2016a). Impact of ground and wheel boundary conditions on numerical simulation of the high-speed train aerodynamic performance. *Journal of Fluids and Structures* 61, 249-261.
- Zhang, J., K. He, X. Xiong, J. Wang and G. Gao (2017). Numerical Simulation with a DES Approach for a High-Speed Train Subjected to the Crosswind. *Journal of Applied Fluid Mechanics* 10(5), 1329-1342.
- Zhang, J., J. B. Wang, Q. X. Wang, X. H. Xiong and G. J. Gao (2018). A study of the influence of bogie cut outs' angles on the aerodynamic performance of a high-speed train. *Journal of Wind Engineering and Industrial Aerodynamics* 175, 153-168.
- Zhang, J. P. and L. Xiang (2019a). Research on development and trend of high-speed train exterior design of China. *Journal of Machine Design* 36, 127-132.
- Zhang, L., J. Y. Zhang, T. Li and W. H. Zhang (2016b). Multi-objective Aerodynamic Optimization Design for Head Shape of High-Speed Trains. *Journal of Southwest Jiaotong University* 51, 1055-1063.
- Zhang, L. F., Z. Sheng, L. Sun and X. J. Liu (2016c). Research on product form design

P. Ji *et al.* / *JAFM*, Vol. 16, No. 1, pp. 193-204, 2023.

based on gene network. *Journal of Zhejiang University of Technology* 44, 584-590.

Zhang, W. Z., J. Lu, W. J. Pan, H. L. Zhao and Z. H. Liu (2019b). Research on Multi-objective Driven Product Morphology Gene Network

Model. *Journal of Graphics* 40, 335-343.

Zhang, Y., Y. Li, J. Li and P. J. Shi (2013). From characteristic line to high-speed train model design. *Machinery Design and Research* 29, 68-71.